Journal of Materials Science: Materials in Electronics (2018) 29:14710–14722
https://doi.org/10.1007/s10854-018-9608-9

Enhanced photoelectrochemical performance of hydrothermally grown tetravalent impurity (Si^{4+}) doped zinc oxide nanostructures for solar water splitting applications

Akash Sharma[1,2] · Mohua Chakraborty[1,2,3] · R. Thangavel[1,2]

Received: 23 May 2018 / Accepted: 5 July 2018 / Published online: 7 July 2018
© Springer Science+Business Media, LLC, part of Springer Nature 2018

Abstract

We report the photoelectrochemical performance of Si-doped ZnO nanorods (NRs) synthesized via two step sol–gel and hydrothermal technique. In the X-ray diffraction patterns the prominent (002) peak confirms the hexagonal wurtzite phase for all samples. In addition to this, the Field Emission Scanning Electron Microscopy images also confirm the hexagonal shape of the NRs with the inclusion of this group IV dopant. The absorption spectra clearly indicates the increase in absorbance in the visible region after doping Si as compared with the undoped ZnO NRs. Bandgap tuning has been noted to be possible after doping. With the insertion of Si^{4+} ion into the ZnO matrix, the oxygen defects acting as recombination centers are reduced, as observed from the photoluminescence (PL) spectrum. We obtain a photocurrent density of 1.101 mA cm^{-2} values (approximately 4.5 times higher than the ZnO sample) at + 0.438 V in presence of 0.1 M NaOH electrolyte solution under visible light illumination (AM 1.5G) for the 8% Si-doped ZnO NRs sample. We attribute this enhancement to the reduction in recombination centers causing suppression of electron–hole recombination due to the reduced oxygen defects as observed in the PL spectrum. The enhanced absorption along with higher surface area of the NRs also promoted the increase in photocurrent value for this Si doped sample. The stability tests conceived that the doped ZnO NRs samples can better behave as a promising photoelectrode material for further generation of clean green energy.

1 Introduction

The increased quest for renewable energy has attracted immense attention of numerous researchers for efficient conversion of solar energy into some useful form of energy. Storing solar energy in the form of chemical bonds is one of the most preferred approaches to solve the energy crisis in the similar fashion as done by nature in case of photosynthesis [1]. In view of this, photoelectrochemistry has been considered to provide a unique and efficient way for the conversion of solar energy into preferred chemical energy [2].

✉ R. Thangavel
rthangavel@iitism.ac.in

1 Solar Energy Research Laboratory, Department of Applied Physics, Indian Institute of Technology (Indian School of Mines), Dhanbad, Jharkhand 826004, India

2 Centre of Excellence in Renewable Energy, Indian Institute of Technology (Indian School of Mines), Dhanbad, Jharkhand 826004, India

3 Indian Institute of Science Education and Research (IISER) Kolkata, Mohanpur, West Bengal, India

By means of photo-induced electrolysis of water, hydrogen can be produced at semiconductor/electrolyte interfaces, which can later be used as fuel. This concept has been privileged because of two important facts i.e., firstly the abundance of sunlight, essential for carrying out the process and secondly the formation of water, the only by-product after combustion of hydrogen. Photoelectrochemical (PEC) water splitting cells are thereof best known for their ability in the conversion of solar energy to consumable fuel by splitting water into nascent hydrogen and oxygen. Moreover, a liquid junction PEC cell owes a special interest in research as it provides a quite simpler way to assemble the cell upon insertion of the semiconductor electrode in a solution [3]. Typically, it consists of a semiconductor photoelectrode to generate electron–hole pair upon illumination along with a reference and counter electrode.

Till date, several materials have been reported for their best suitability in solar water splitting applications [4]. In view of the above, oxides are always preferred for this purpose due to their environmentally benign nature. Some oxides like ZnO [5, 6], Cu_2O [7, 8], TiO_2 [9, 10], WO_3 [11, 12], $BiVO_4$ [13, 14],α-Fe_2O_3 [2, 15] etc. have been proven

most reliable for solar water splitting applications. Properties like nontoxicity, cost-effectiveness, stability have given preference to these materials for photoelectrochemical applications. But some drawbacks like structural defects, limitation in light absorptivity, poor stability in aqueous medium and enormously short recombination time are associated with these materials which result in reduced efficiency [16]. Among the above oxide materials, ZnO has been noted to be widely investigated due to its superiority over others. It is a well-known n-type material with a wide bandgap of nearly 3.2 eV, direct band structure, large exciton binding energy of 60 meV at room temperature. As a photoactive material, properties like high electron mobility, electron transfer efficiency along with abundant morphologies, simple tailoring of nanostructures and favorable environmental compatibility proves its strong candidature. Beyond this ZnO has also wide range of applications in optoelectronics, sensing devices etc. [17–19]. Its suitable band positions i.e. conduction band minimum at − 0.31 V and valence band maximum at + 2.89 V (both values were measured w.r.t Normal Hydrogen Electrode (NHE)), proves its credibility for water oxidation (1.23 V vs. NHE) [20].

Despite of these physical and chemical properties, ZnO has several drawbacks that makes its candidature feeble as a photoactive material. Firstly, being a UV active material it is able to use only 4% of the solar spectrum which is very less as compared with visible light (43%) [21]. Secondly, the photocorrosion of ZnO in case of long-term photocatalytic reactions also put hurdles in its commercialization [16]. Besides this, the fast surface recombination rate of photoinduced electron–hole pairs also restricts the efficiency. For suitable photoactivity, a material should be capable of efficient charge collection followed by separation and transfer to the surrounding medium. In case of nanorods (NRs), their large surface area-to-volume ratio takes the advantage by providing a large interface area to the surrounding electrolyte medium. This helps the minority carrier to diffuse through the interface making an efficient charge separation possible. Not only this but also in order to achieve high photocurrents, the hole should leave the interface easily so the diameters can be controlled which may suffice the hole diffusion length [22]. Therefore, these one-dimensional structures have emerged as a reliable candidate for photoelectrochemical efficiency enhancement.

Several synthesis techniques, like chemical vapor deposition [23, 24], magnetron sputtering [25], pulsed laser deposition [26], atomic layer deposition [27], electrodeposition [28], spray pyrolysis [29] and hydrothermal [30] have been reported till date for the fabrication of ZnO NRs. However, in light of its simplicity, cost-effectiveness, large area deposition, and flexibility in the compositional modification, the hydrothermal method has pervasively being used for commercialization. Besides this the use of low temperature for this report was desirable in order to avoid any other secondary phases.

ZnO being a wide bandgap metal oxide semiconductor suffers with the loss of photoactive electron hole pair due to recombination and causes adverse effects on the photoactivity [31]. Incorporation of several dopants into the ZnO host matrix have proved beneficial for enhancement of better physical properties [32]. In view of the chemical stability issues of photoelectrodes, basically two types of approaches are followed in real photoelectrochemical systems. Firstly deposition of a conductive as well as protective layer to tackle the issues with corrosion during reaction and secondly the development of new methods such as surface modification, formation of heterostructures etc [33, 34]. Several groups have reported the use of metal oxides such as SiO_2, TiO_2, Al_2O_3 as capping agents for the ZnO nanostructures in order to gain better chemical stability [16, 35]. We believe that with the inclusion of Si in ZnO nanostructures, better photostability can be conceived for the one dimensional nanostructures. Si has been a notable dopant and occupies the cation site in III–V semiconductors for enhancement of both optical and electrical properties. Not only this could help in enhancing the physical properties but also it will prove its usefulness in Si-related devices. An intermediate phase of Zn_2SiO_4 is obtained upon insertion of Si in ZnO mostly at high temperatures [36], as both Zn and Si possess several similarities in terms of electronegativity (1.65 and 1.9) and atomic radius (0.133 and 0.117 nm) [37]. Thus it has remained a challenge to use Si as a dopant for ZnO NRs.

A very few reports are available with ZnO NRs doped with Si [38, 39]. Minami et al. have reported that by using Si; a group IV element as a dopant causes a decrease in resistivity and increase in transmittance of the films [40]. It has also been reported earlier that with substitution of Si in ZnO lattice, it can more likely happen that Si will replace Zn owing to the low defect formation energy and acts as a n-type semiconductor [41, 42]. Here in this article we have doped Si via a low cost, solution based approach which showed improvement in doping percentage along with physical properties as compared with earlier reported literature [43].This can be further helpful in the fabrication of solar cells to serve as a bottom contact. In this study, we for the first time have investigated the photoelectrochemical performance of ZnO NRs after doping Si. This result can help to fabricate suitable photoelectrodes for application in PEC cells. Owing to its resistivity and transparency, it may also prove beneficial for tandem structures in light of solar water splitting as well as other photovoltaic applications. Furthermore, the stability of ZnO NRs after doping is investigated which can help in further fabrication of stable photoelectrodes.

2 Experimental details

2.1 Materials

Zinc acetate dihydrate ($Zn(CH_3COO)_2·2H_2O$, 98% purity), Monoethanolamine (C_2H_7NO, 98% purity), Zinc nitrate hexahydrate ($Zn(NO_3)_2·6H_2O$, 98% purity), Hexamethylenetetramine ($C_6H_{12}N_4$, 99% purity), Sulphuric Acid (H_2SO_4, Emparta ACS grade, 98% purity), Acetone (C_3H_6O,Emplura grade, 99% purity), 2-propanol (C_3H_8O, Emplura grade, 99% purity), Hydrogen Peroxide (H_2O_2, Emparta grade, 30% purity) from Merck Chemicals; 2-Methoxyethanol ($C_3H_8O_2$, 99% purity) and Tetraethoxysilane (TEOS) ($C_8H_{20}O_4Si$, 99% purity) were purchased from Alfa Aesar Chemicals respectively and used as received without any further purification. The entire process was carried out with deionized water (DI water) wherever the experiment necessitates.

Standard procedure was followed for substrate cleaning. The glass substrates were cut with an area of (1×1) cm^2. These were ultrasonicated with different solutions during the cleaning process with specified time duration. In the beginning, Piranha solution (H_2SO_4:H_2O_2::3:1) was used for 02 h to create a rough surface for better deposition of thin films. Subsequently, the substrates were treated with acetone and ethanol followed by DI water after each successive step for 20 min. These glass substrates were further dried in a hot air oven for a duration of 03 h. Finally, the samples were treated with nitrogen gas for 10 min before coating.

2.2 Synthesis of photoelectrodes

All the ZnO NRs samples were synthesized via sol–gel, spin coating and hydrothermal method as reported elsewhere through a two-step procedure [44, 45]. First is deposition of the seed layer on cleaned substrates and in second step NRs are grown by dipping the seed layers in growth solution. All the growth conditions including the growth temperature were kept at 90 °C for 5 h as per our earlier reports [45]. Tetraethoxysilane has been used as a Si dopant precursor. A separate solution was prepared for each concentration by dissolving Si precursor in DI water as required, ranging from 2.0 to 8.0 molar %. Finally, the dopant solution was added dropwise into the growth solution containing hexamethylenetetramine and zinc nitrate hexahydrate as per the desired concentration. The Si-doped ZnO NR arrays were prepared in the similar fashion as mentioned earlier for undoped ones. Finally, the prepared films were rinsed with DI water followed by drying at room temperature. The samples grown with several doping percentages i.e. 0, 2, 4, 6 and 8%; are hereafter named as ZnO, 2SZO, 4SZO, 6SZO and 8SZO respectively.

2.3 Characterization techniques

The crystallinity of all the nanostructured samples were examined via a X-Ray diffractometer (PANalytical Empyrean model) using monochromatic $CuK_{\alpha1}$ radiation ($\lambda = 1.5406$ Å). The surface morphologies of the NRs were visualised by using Field Emission Scanning Electron Microscopy (FESEM) (ZEISS Supra 55 model). The optical parameters of the nanostructures were enunciated from the absorption spectra by means of an UV–Vis-NIR double beam spectrophotometer (Agilent Cary 5000 model). Photoluminescence and time-resolved photoluminescence measurements were carried out by using a Cary Eclipse fluorescence spectrophotometer (Agilent Technologies). The Hall measurements were carried out by using a Hall Effect measurement set up (Ecopia Model) at Inter-University Accelerator Centre (IUAC), New Delhi, India. For photoelectrochemical measurements, a customized three-electrode cell configuration consisting of a Pt sheet, an Ag/AgCl (saturated with KCl) and grown nanostructured thin films as a counter, reference and working electrodes, respectively have been used. An aqueous solution of 0.1 M NaOH has served the role of an electrolyte. The electrode potential was varied from − 0.5 to + 1.0 V using a potentiostat (Princeton EG & G Applied Research). In order to create suitable light and dark conditions, the samples were illuminated by using an Oriel AM 1.5G filtered Xenon arc lamp with the intensity set to 100 mW cm^{-2}.

3 Results and discussion

3.1 Structural properties

Figure 1 depicts the X-ray diffraction (XRD) patterns of all the hydrothermally grown doped and undoped ZnO NRs. From the diffraction patterns, the characteristic diffraction peak (002) of the ZnO NRs can be clearly seen which verifies the hexagonal wurtzite structure (JCPDS card no.36-1451, space group $P6_3mc$) [15]. The prominent diffraction peak observed for (002) plane in ZnO NRs were stronger than those from other planes. Thus the crystal has growth along c-axis based on the strongest, characteristic (002) diffraction peak, and is also in suitable agreement with earlier reported literature [15]. The shifting of (002) peak towards higher 2θ values has occurred for an increase in dopant concentration and clearly represented in Fig. 1. Due to the substitution of lower ionic radius Si^{4+} (0.04 nm) as compared to Zn^{2+} (0.074 nm) in ZnO host lattice, the crystal plane spacing shrinks causing reduction in cell volume as well as shifting of (002) peak towards higher angle side [27, 46, 47]. The average crystallite size

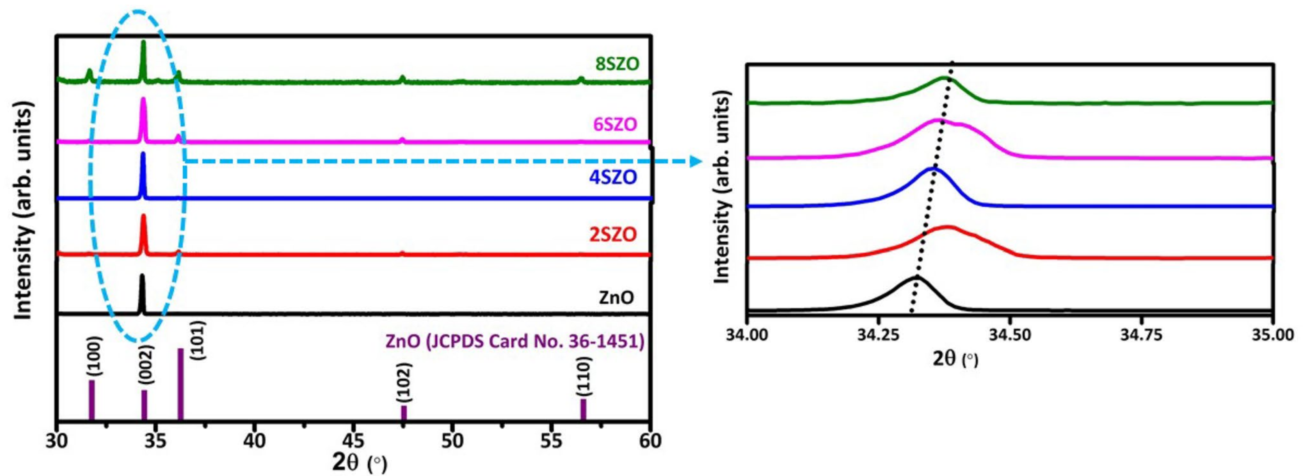

Fig. 1 XRD patterns of as-prepared ZnO NRs and Si-doped ZnO NRs along with the magnified XRD pattern representing the higher angle shifting of (002) peak with increase in doping concentration

was calculated using the Debye–Scherrer's formula represented in Eq. (1). The dislocation density was estimated from the Eq. (2).

$$D = \frac{0.9\,\lambda}{\beta\cos\theta} \tag{1}$$

$$\delta = \frac{1}{D^2} \tag{2}$$

The lattice constants were calculated using the following equations as reported earlier [28, 47],

$$a = \frac{\lambda}{\sqrt{3}\,\sin\theta} \tag{3}$$

$$c = \frac{\lambda}{\sin\,\theta} \tag{4}$$

where λ is the wavelength of $CuK_{\alpha 1}$ radiation used (=1.5406 Å), and θ is the angle of diffraction. The variation in length of c-axis of the ZnO NRs are attributable to Si^{4+} ions occupying the Zn sites in the wurtzite crystal structure. It can be better understood as, when the Si^{4+} ions tries to replace Zn^{2+}, it creates cationic vacancies due to the electrical neutrality of ZnO crystal (as given in the mechanism below) [48].

$$2Zn^{2+} \rightarrow Si^{4+} + V_{Zn}^{2+} \tag{5}$$

Thus the reduction of c-axis length as well as higher angle shifting of the (002) peak position indicates that Si^{4+} ion has occupied the substitutional positions of Zn^{2+} leading towards structural deformations and stress within the ZnO host matrix. The stress induced in the ZnO matrix by the incorporation of Si^{4+} ion was estimated using Eq. 6 and represented in Table 1.

$$\sigma = -453.6 \times 10^{9}\left\{\frac{c_0 - c}{c_0}\right\} \tag{6}$$

where cis the lattice constant obtained from the (002) diffraction peak and c_0 is 5.205 Å for bulk ZnO. It was also observed that the doping has caused an increase in the FWHM values of (002) peak as compared with the undoped ZnO NRs sample. Thus it can also be conceived that the

Table 1 The structural parameters calculated from XRD

Sample	2θ at (002) plane (°)	c (Å)	a (Å)	Crystallite size (nm)	Stress σ (×10^9) (N m^{-2})	Dislocation density (×10^{-3}) $(nm)^{-2}$
ZnO	34.3136	0.522259	0.301535	92.86	− 0.667546	0.115955
2SZO	34.38006	0.52128	0.30097	60.35	− 0.865369	0.274596
4SZO	34.34635	0.521776	0.301257	90.31	− 0.773865	0.122606
6SZO	34.37274	0.521388	0.301032	59.03	− 1.111995	0.28702
8SZO	34.3656	0.521493	0.301093	89.26	− 0.679746	0.125513

Crystallite size was calculated using Debye–Scherrer's formula

crystallinity of the NRs decreases upon doping. Among all the samples only 2SZO shows an exception of excess shifting of (002) peak. It can be better conceived that stoichiometric modification of the film with Si addition or existence of lower oxidation state of Si are the prime causes for this shift concluding with variation of c-parameter [49]. Meanwhile the tetravalent impurity after being integrated into the host matrix has caused in the rise of asymmetric peaks in case of some samples. As reported by several groups the asymmetric nature may would have occurred due to the anisotropic shrinkage of lattices, which leads to lattice distortion [50, 51]. Furthermore, Chason et al. suggested that during the growth of nanostructures, there occurs transition from incremental tensile to compressive stress even if the growth rate is assumed to be constant which was observed to be in agreement with our experimental results [52].

3.2 Morphological properties

Figure 2a–j represents the top view and cross sectional view field emission scanning electron microscopy (FESEM) images of undoped and Si-doped ZnO NRs. All the FESEM images were analyzed using ImageJ software. From the top view images all the samples were observed to be well contained with vertically aligned hexagonal NRs in a regular manner on the substrate. The effect of Si concentration on

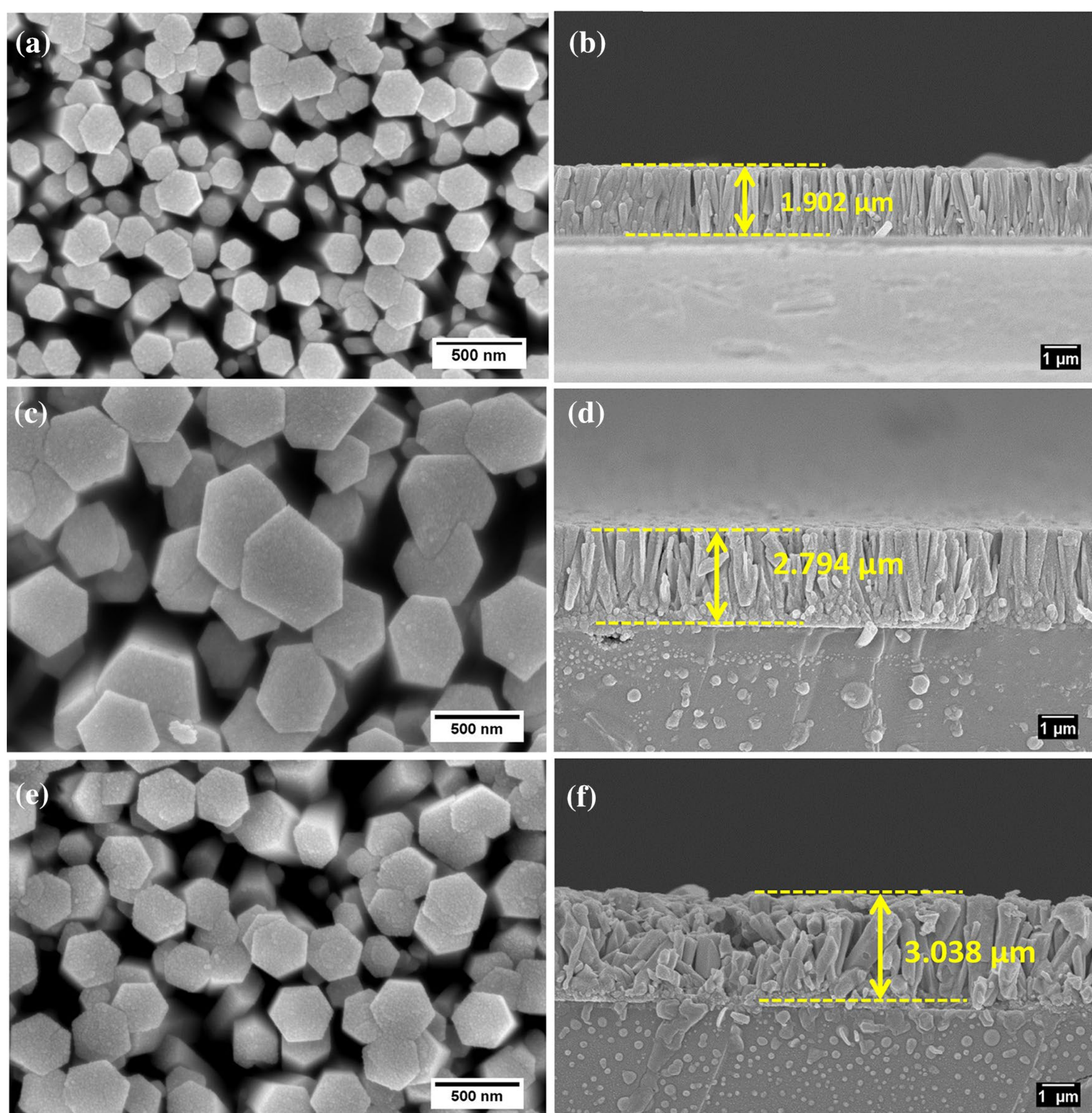

Fig. 2 Top view and typical cross sectional view FESEM images of (**a, b**) ZnO NRs, (**c, d**) 2SZO, (**e, f**) 4SZO, (**g, h**) 6SZO, (**i, j**) 8SZO samples at 500 nm and 1 µm scale respectively; (**k**) Graph showing variation in diameter and length of all the samples along with change of Si doping concentration

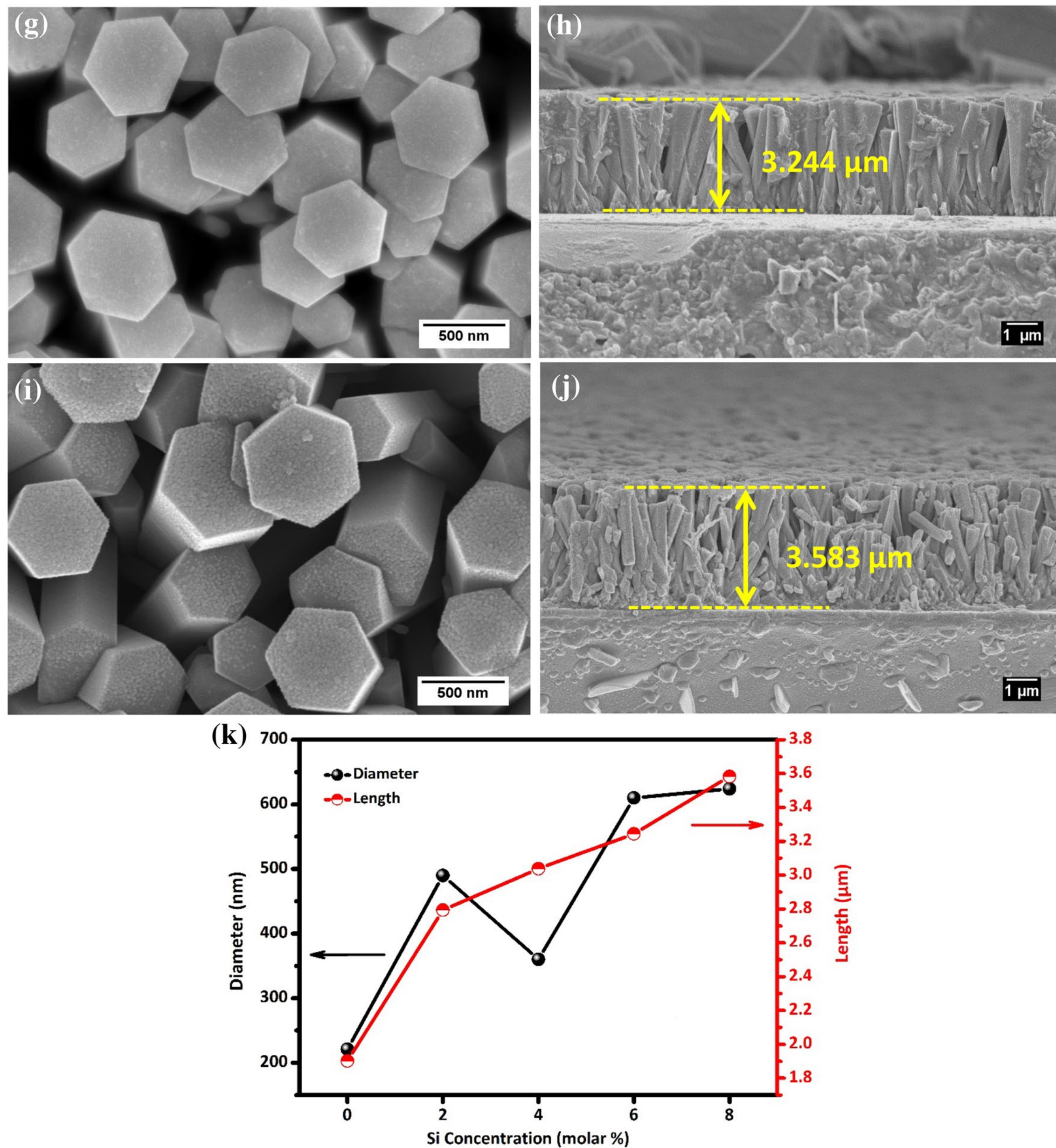

Fig. 2 (continued)

the morphology can be clearly visualized in the images. Upon doping Si with ZnO, all the sampes showed an increase in the diameter as compared with the undoped sample (221 nm). The diameters of the nanorods were observed to vary within the range of 220–630 nm. As TEOS (Si precursor) is easily soluble in water and forms SiO_2 along with methanol so we cannot completely neglect its presence during the syntheis procedure. Due to the stability of SiO_2 it remains inactive within the growth solution and the number of dopant ions available to replace Zn^{2+} decreases. We understand the random variation in the diameter values of SZO samples has occurred because of these charge carriers. The variation in the diameters are caused due to the replacement of Zn^{2+} by the Si^{4+} ion at the interstitial positions. These results were also in agreement with the carrier concentration values obtained from Hall effect experiment and described in Table 2. Because of this possible reason the 4SZO sample shows out of the trend behaviour as compared to the other samples. With the addition of Si, the hexagonal structure has been maintained for all the sample. But with a subsequent increase in concentration the shape of the rods becomes prominent.

It can also be clearly noted that the NRs density (defined as number of nanorods per unit area) has decreased upon

Table 2 The average diameter as well as length were calculated from FESEM. The carrier concentration was measured from the Hall effect set up

Sample	Average diameter (nm)	Length (μm)	Carrier concentration (cm)$^{-3}$ (× 10^{15})
ZnO	221	1.902	0.5523
2SZO	490	2.794	76.85
4SZO	360	3.038	66.17
6SZO	610	3.244	108.6
8SZO	624	3.583	131.14

increase in doping concentration. Not only this but also the lengths of the NRs were found to be increased after doping Si. Figure 2k presents the variation in diameters as well as length of the NRs with change in Si doping concentration. It has been reported earlier that the higher values of diameters shows absence of surface effects at least for minority charge carriers in n-type semiconductors [22, 53]. It can be proved advantageous as the surface recombination has a significant impact in reducing the photocurrent. Besides this the enhancement in the morphological parameters causes a significant increase in the surface area leading towards better photophysical properties by absorbing most of the solar energy as compared to its undoped counter part [54, 55]. Thus better photoresponse can also be obtained for the NRs with higher diameter and lengths. Only from these results we cannot rule out the presence of surface defects. So in order to get a better clarity regarding the defects as well as their impact on the solar light driven processes, photoluminescence (PL) and photocurrent experiments were carried out.

3.3 Optical properties

The absorption spectra of all the synthesized NRs samples investigated within the spectral range 350–750 nm is represented in Fig. 3. The bandgap values were enunciated from the absorption spectra by means of Tauc's plot and the results so obtained were summarized in Table 3. The absorption band edge for undoped ZnO NRs was obtained at ~ 390 nm. It has also been observed that the absorption percentage is less in the visible light range. Due to the addition of Si, a slight increase in the absorbance values

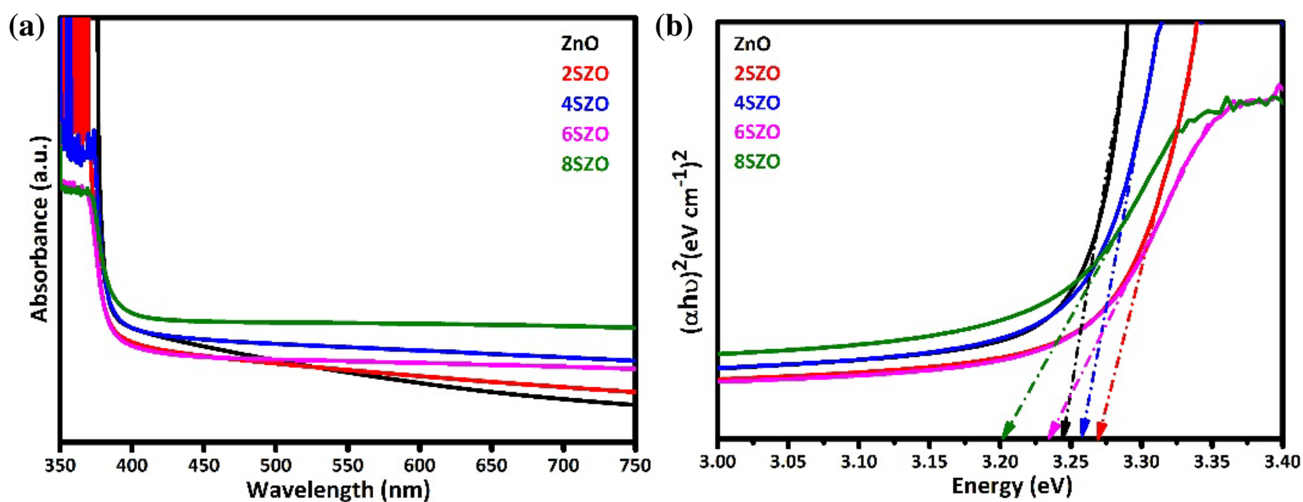

Fig. 3 (**a**) UV–Vis absorption spectra and (**b**) Tauc's plot for all the grown ZnO NRs films

Table 3 The optical band gap, absolute electronegativity and conduction band and valence band level, refractive index, high frequency dielectric constant, static dielectric constant from absorption spectrum results

Sample	Optical band gap (eV)	Absolute electro negativity (χ)	CB level (eV)	VB level (eV)	Refractive index (n)	High frequency dielectric constant(ϵ_∞)	Static dielectric constant (ϵ_0)
ZnO	3.240	5.792495145	− 0.327504855	2.912495145	2.4028	5.7735	8.5408
2SZO	3.268	5.796518978	− 0.337481022	2.930518978	2.3976	5.7487	8.45456
4SZO	3.250	5.800545607	− 0.324454393	2.925545607	2.4010	5.7646	8.51
6SZO	3.220	5.804575033	− 0.305424967	2.914575033	2.4065	5.7914	8.6024
8SZO	3.189	5.808607258	− 0.285892742	2.903107258	2.4123	5.8948	8.69788

in visible range has been observed. Tunable bandgap property of the as-grown nanostructures has evolved because of replacing Zn^{2+} ion by Si^{4+} ion. With 2% Si-doping, the bandgap value showed an increase from 3.24 to 3.268 eV. But afterward as we go on increasing the concentration a constant decrement is observed (shown in Table 3). The conduction band, as well as valence band levels, were calculated theoretically in case of all the ZnO NRs samples as reported earlier [47] and summarized in Table 3. The increment in bandgap values observed with the 2SZO sample can be explained by Burstein- Moss (BM) effect [56]. It states that in an intrinsic semiconductor, the fermi level lies below the conduction band and upon an increase in the concentration of charge carriers it gets shifted above, which causes a blue shift of bandgap. With the increase in the addition of tetravalent impurity further a clear reduction of bandgap has been observed, which has been considered due to the new ion (Si^{4+}) energy level formed within the valence band and conduction band. Further the increase in the concentration of carriers is also being clearly indicated by the interstitial zinc atoms or oxygen vacancies at room temperature. Along with the increase in electron concentration due to subsequent doping of Si^{4+}, charge carriers move randomly as well as gets scattered upon striking with ionized impurities. This causes in modification of electronic states, which plays the major role in decrease of bandgap. Thus many body effects like exchange and Coulomb interactions overcomes the Burstein–Moss effect [57].

The refractive index (n) and dielectric constant (ϵ)of a semiconducting material play an important role in determining the optical and electrical properties. The refractive index of all the samples was calculated using Moss relation [58].

$$E_g n^4 = 108\,\text{eV} \tag{7}$$

Both static and high-frequency dielectric constant values were further worked out for all the samples using the following equations and represented in Table 3.

$$\varepsilon_\infty = n^2 \tag{8}$$

$$\varepsilon_0 = 18.52 - 3.08E_g \tag{9}$$

It can be clearly concluded that the polarising ability of 8SZO is highest as compared with the rest samples. Furthermore, the static dielectric constant values indicate that at a low frequency or constant electric field the highest doped sample gives better results.

PL spectroscopy provides a wide scope for the analysis of the essential radiative processes (recombination or separation) of the photogenerated electron–hole pairs being carried out within the semiconductor. More or less the PL spectra of ZnO consists of two major peaks. First one is the UV emission, also named as near band edge (NBE) emission centered approximately at 390 nm and the second one is a broad peak also called as the deep level emissions (DLE) in the visible range [59]. A detailed analysis of this has been reported earlier [47]. Figure 4a represents the room temperature PL spectra of all the SZO samples as a function of concentration with excitation at a wavelength of 320 nm. All the samples were observed to possess a broad peak in the visible range, ranging from 475 to 675 nm. This is usually attributed to the singly ionized oxygen vacancies$\left(V_O^+\right)$ and considered responsible for green emission in DLE. From Fig. 4a, it can be clearly inferred that the Si dopant percentage is inversely proportional to the PL intensity of green emission peak and subsequently for 8SZO attended the lowest value. These variations in intensity can also be seen as the effect of successful incorporation of Si^{4+} ion into the ZnO host matrix. The weak emission as seen from the PL graph for the 8SZO shows that the sample is in possession with the lowest surface defect as compared with the other doped samples. Furthermore, lesser the defects, fewer recombination centers are present causing a better electron flow pathway [60]. Due to the wide unavailability of recombination centers, which acts like energy barriers at the interface causes the photoelectrons and holes to stay separated for a comparatively longer duration. Subsequently resulting in efficient charge separation leading to increment in current density values and hence improvement in the PEC performances. In order to study the role of oxygen vacancy on photoelectrochemical efficiency, all the nanostructures were treated in a similar electrochemical environment using a three-electrode system under appropriate dark and illumination conditions. Figure 4b represents the time-resolved photoluminescence spectra of all the ZnO and SZO samples. To elucidate the carrier life time, the decay curves were fit monoexponentially (shown in Fig. 4c–g). After fitting the curve, a better carrier lifetime of 0.09427 ms was observed for the 8SZO sample as compared with ZnO (0.05314 ms).

3.4 Photoelectrochemical properties

In order to evaluate the photoperformance of each photoanode the photocurrent density generated was measured by irradiating from the front (semiconductor to substrate) side of the film while being immersed in electrolyte solutions. Figure 5 represents the photoelectrochemical behavior of all the samples (photoelectrodes), observed in both dark and illumination conditions by means of a three electrode photoelectrochemical cell (PEC) in presence of 0.1 M NaOH (pH = 13). For undoped ZnO NRs a photocurrent density value of ~ 0.245 mA cm^{-2} was observed as compared with 0.0038 mA cm^{-2} (in dark) at + 0.438 V (vs. Ag/AgCl). Further, upon illumination the photoresponse values showed notable enhancement along with increase in the dopant concentration. The highest photocurrent density of nearly

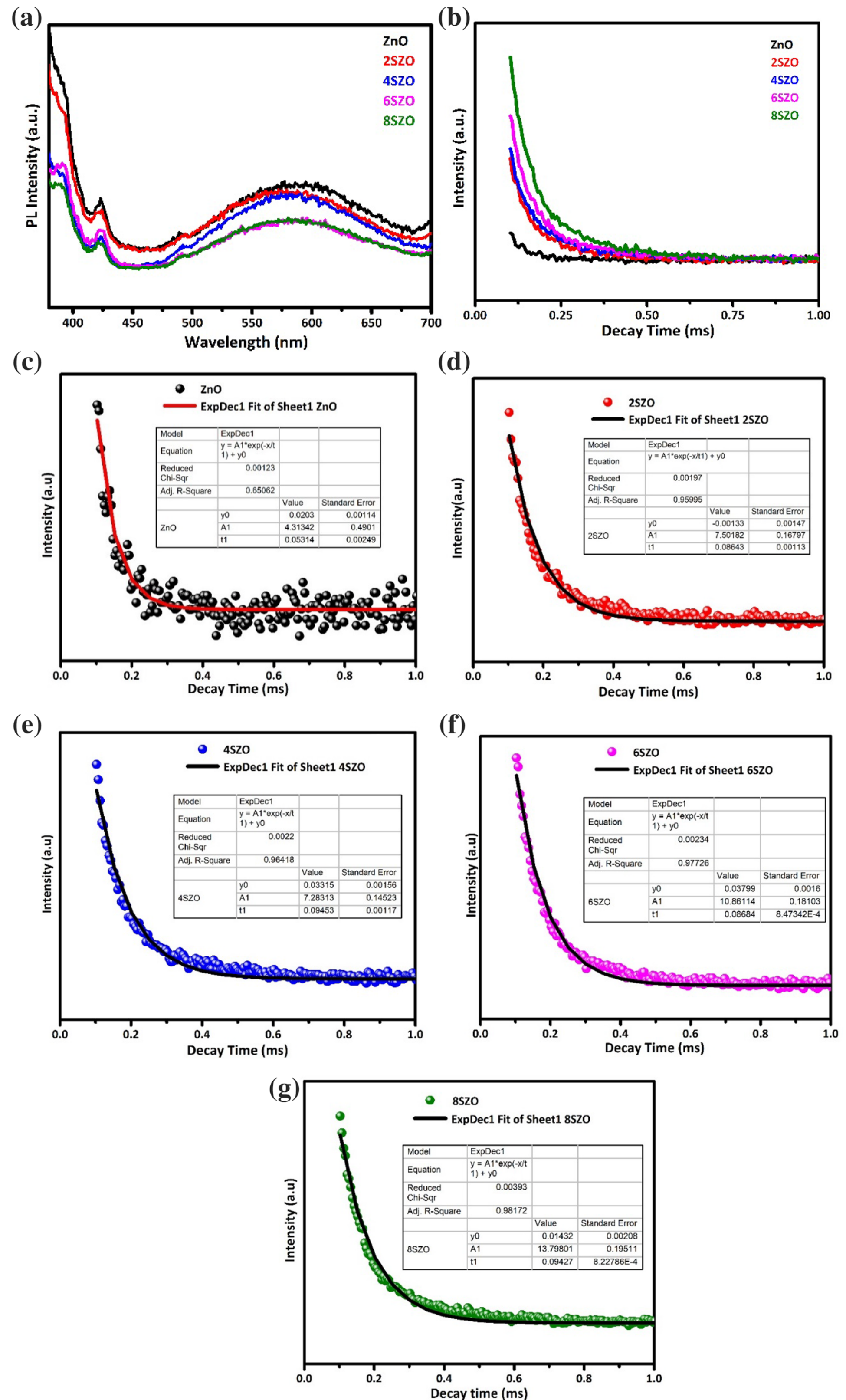

Fig. 4 (**a**) The photoluminescence spectra. (**b**) Time-resolved photoluminescence spectra of undoped and Si-doped ZnO NRs films. (**c**–**g**) Monoexponentially fitted decay curves for all the samples

1.101 mA cm^{-2} was observed for the 8SZO photoelectrode. Further an enhancement factor of nearly 350, 110, 77 and 32% were obtained for the undoped ZnO (0.245 mA cm^{-2}), 2SZO (0.525 mA cm^{-2}), 4SZO (0.622 mA cm^{-2}) and 6SZO (0.829 mA cm^{-2}) samples respectively as compared with the highest obtained photocurrent for 8SZO sample. Among

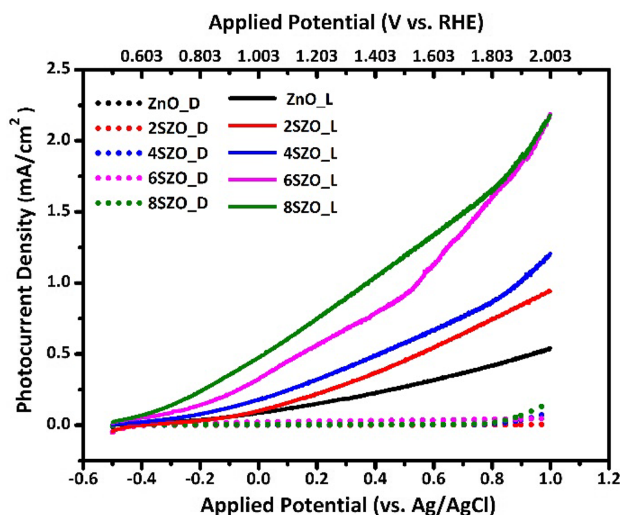

Fig. 5 Photocurrent density (mA cm^{-2}) versus applied potential (vs. Ag/AgCl) measurements of undoped ZnO NRs and Si-doped ZnO NRs films under dark and visible light illumination at room temperature in 0.1 M NaOH electrolyte solution

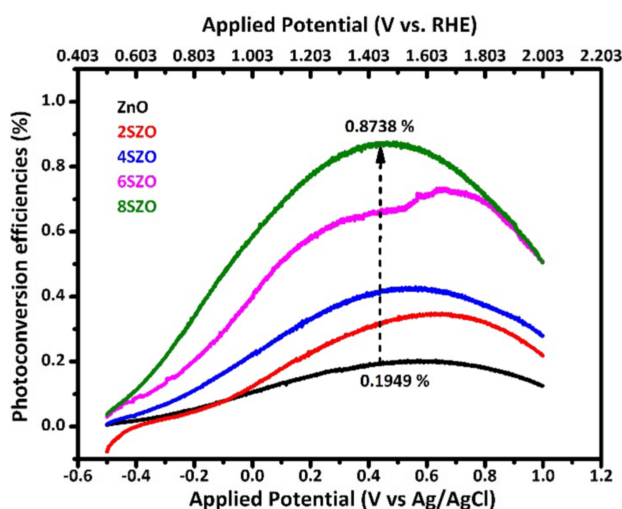

Fig. 6 PCE (%) for undoped ZnO NRs and Si-doped ZnO NRs films under dark and visible light illumination at room temperature using 0.1 M NaOH as an electrolyte solution

all the samples, the immediate photocurrent generation at lower potential values of 8SZO sample indicates the superior PEC properties. It can be clearly remarked that the increase in photoabsorption as well as reduction in surface defects have supported the increase in photocurrent density after the insertion of Si in ZnO host matrix. Furthermore, the separation of photogenerated electron–hole pairs also occurs more effectively at the semiconductor/electrolyte interface. This infers that, there is a decrease in the recombination probability, which is also in agreement with our PL results (shown in Fig. 4a). Again the inclusion of Si, has more likely caused the increase in surface area, and a better photoconductivity as well.

The photoconversion efficiency (PCE) (η) for photoanodes was estimated by using the Eq. (10). Though the equation is meant for the two-electrode system it has been assumed that the same current–voltage behavior is observed for our three-electrode system, relying on this concept we have used this for qualitative explanation in a similar way as done by earlier reports [2].

$$\eta(\%) = \frac{\text{Total power output} - \text{electrical input}}{\text{Light power input}} \times 100 = \frac{J_p\left[1.23 - V_{app}\right]}{P_{light}} \times 100 \quad (10)$$

where V_{app}(V) is the applied external potential, J_p is the externally measured current density (mA cm^{-2}) at V_{app} and $P_{light}$is the power density of the incident source of light (mW cm^{-2}). Figure 6 presents the PCE of all the SZO films along with variation in molar concentrations with reference to the undoped ZnO NRs sample. The PCE values estimated for all the samples were represented in Table 4. A significant increase was observed after Si doping on ZnO NRs and for 8SZO sample maximum PCE of 0.8738% was observed, which is approximately 4.5 times higher as compared to undoped ZnO NRs film electrode (0.19404%). The PCE was found to be increasing with subsequent increase in the concentration, which is also well consistent with the photocurrent results.

Furthermore, the stability along with the enhanced photo performance of the photoelectrodes are considered as the critical evaluation factors for industrial application. In regard to this photostability of ZnO has ever remained as a challenge without use of sacrificial agents [31]. ZnO reacts with both acid as well as base due to its amphoteric nature [61, 62]. Again, taking into account the acidic electrolyte medium the etching rate is faster than that of the later [63].

Table 4 Photocurrent and photocurrent density values along with enhancement percentage (δ%) due to illumination from LSV measurements. Photo conversion efficiency of Si-doped ZnO nanorods

Sample	Photocurrent density (mA cm^{-2}) at +0.438 V from LSV curve			PCE (%)
	Dark (J_D)	Illumination (J_L)	δ (%)	
ZnO	0.00379	0.245	349.388	0.194
2SZO	0.00259	0.525	109.714	0.416
4SZO	0.00449	0.622	77.010	0.493
6SZO	0.0331	0.829	32.811	0.656
8SZO	0.00501	1.101	–	0.873

ZnO as a photoanode suffers with two types of decomposition. Firstly the cathodic decomposition and second one is the photoanodic decomposition [61, 63].

Cathodic decomposition:

$$ZnO + 2e^- + 2H^+ \rightarrow Zn + H_2O \quad (11)$$

Photoanodic decomposition:

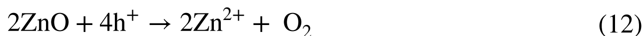

$$2ZnO + 4h^+ \rightarrow 2Zn^{2+} + O_2 \quad (12)$$

In this present case, we have focussed on the cathodic decomposition of the samples. In order to study the photoelectrochemical stability of Si-doped ZnO NRs, the samples after PEC measurement under dark and illumination conditions (described earlier) were examined under FESEM. Figure 7a–d represents the top view images of the SZO samples at several scales after the experiment. After a typical scan and tested under illumination conditions within the potential window of − 0.5 to + 1.0 V (vs. Ag/AgCl) in presence of 0.1 M NaOH for 30 min, the images were collected. For a better understanding, an attempt was being made to collect the images containing both the untreated as well as electrolyte-dipped regions. In all Fig. 7a–d the variation can be clearly observed, where the NRs structure is moderately maintained even if after the experiment. All the samples were found to possess moderate stability. All the aforementioned samples faced a minimal damage, which can be better treated as stable photoelectrodes. This highlights the stability of the prepared samples upon insertion of Si. The robustness can also be better investigated with other suitable parameters of electrolyte, which is currently beyond the scope of this context. Based on the present study obtained so far the 8SZO sample can be considered as the best one owing to its stability in alkaline medium and highest PEC efficiency (as compared to the other fabricated nanostructured samples).

4 Conclusion

We have described the systematic study of Si-doped ZnO NR samples, synthesized by using low cost facile sol–gel hydrothermal technique. Both XRD and FESEM images were in well agreement with the fact that no structural changes occur for the ZnO nanorods upon doping with Si. The variation in bandgap also provides a scope for bandgap tunability with this dopant. Using Si^{4+} as a dopant caused an enhancement of the photocurrent values due to the more number of electrons reaching the conduction band. A PEC efficiency of 0.87% was also obtained for the 8SZO sample due to the increased photo-absorption owing to its increase in surface

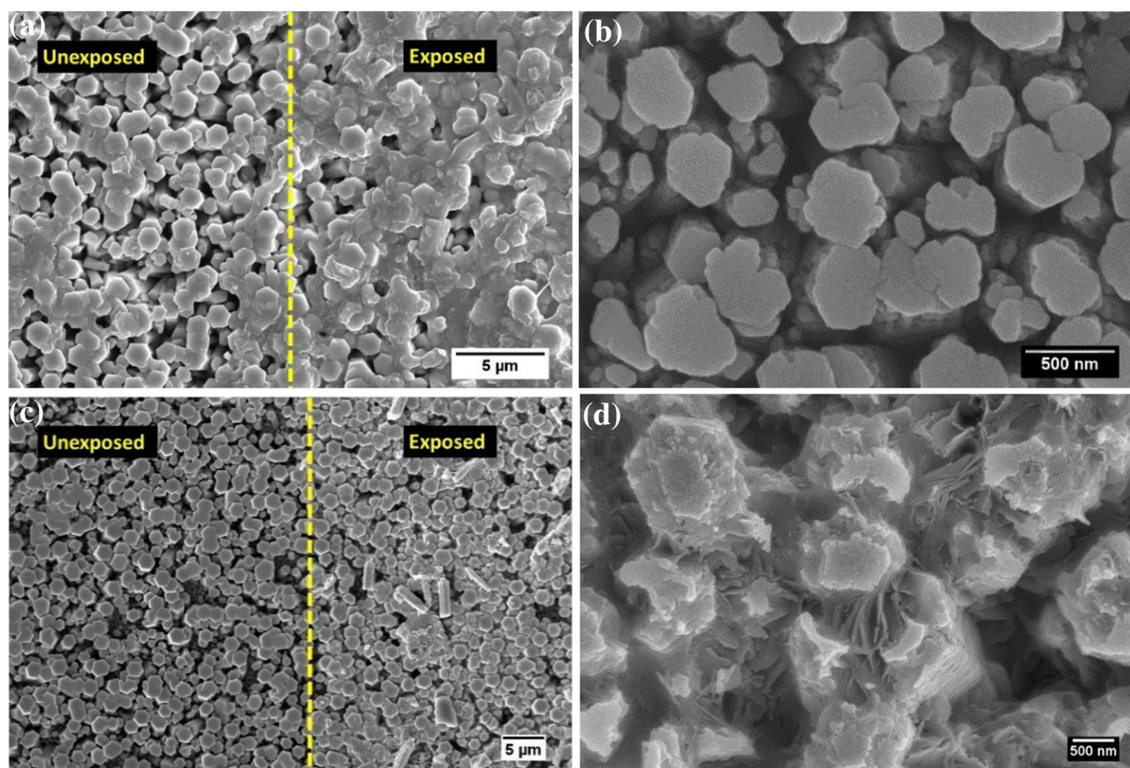

Fig. 7 Top view FESEM images of the all the Si doped ZnO NRs samples after PEC measurement in presence of 0.1 M NaOH in sequence as (**a, b**) 2SZO, (**c, d**) 4SZO, (**e, f**) 6SZO, (**g, h**) 8SZO

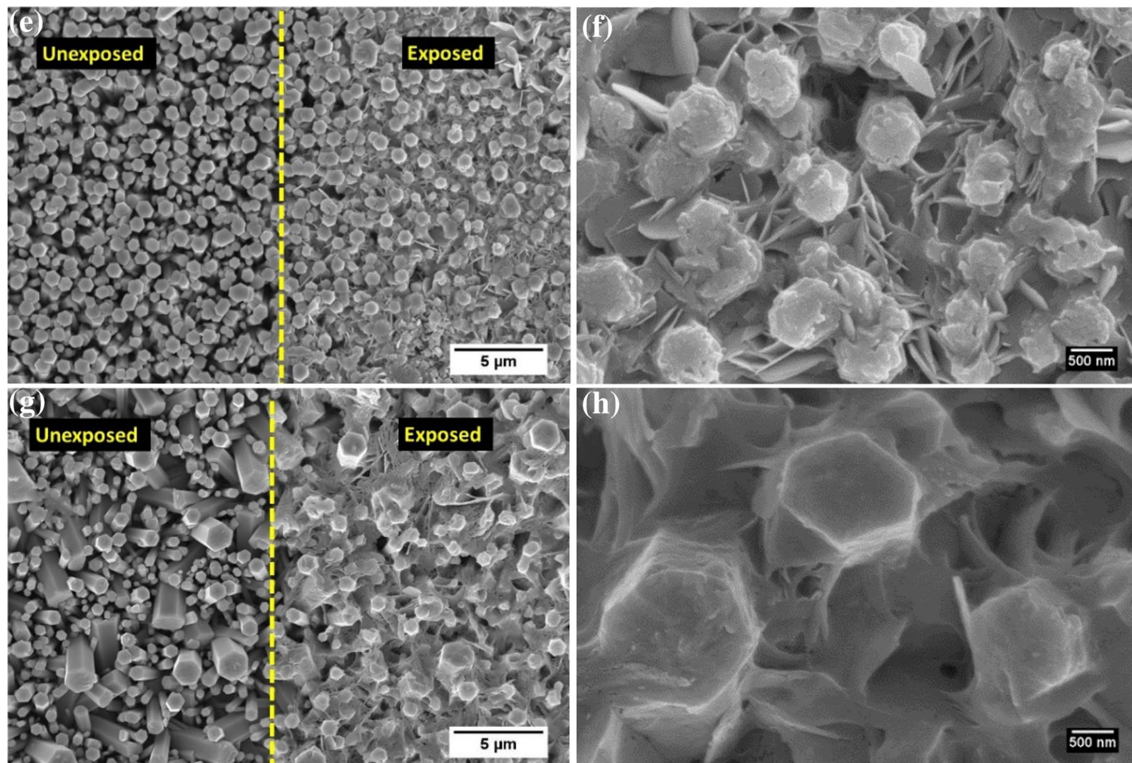

Fig. 7 (continued)

area as well as reduction in surface defects. Finally, the photoelectrochemical stability of this amphoteric metal oxide was discussed. The study revealed that 8SZO sample can be further used with regard to their PCE efficiency and stability to aqueous media.

Acknowledgements The authors acknowledge the Department of Science and Technology (DST) for the project with Grant Number SR/FTP/PS-184/2012, SERB vide Dy. No. SERB/F/5439/2013-14 dated 25.11.2013 and Faculty Research Scheme-FRS (54)/2103-2014/APH. The authors would also like to thank the Ministry of Human Resource and Development project under the Scheme-Establishment of Centre of Excellence for Training and Research in Frontier Areas of Science and Technology (FAST) in Renewable Energy vide letter F. No. 5-5/2014-TS.VII dated 04.09.2014. The authors would like to thank Indian Institute of Technology (Indian School of Mines), Dhanbad, India for providing research fellowship and Central Research Facility (CRF) respectively. We are also thankful to Dr. K. Asokan, Scientist F, Materials Science Division, Inter University Accelerator Centre, New Delhi for his support in carrying out the Hall measurements. One of the authors M.C. would like to acknowledge Indo-US Science and Technology Forum (IUSSTF) for providing international Bhaskara Advanced Solar Energy (BASE-2016) fellowship.

References

1. M.G. Walter, E.L. Warren, J.R. McKone, S.W. Boettcher, Q. Mi, E.A. Santori, N.S. Lewis, Chem. Rev. **110**, 6446 (2010)
2. S.Y. Gurudayal, M.H. Chiam, P.S. Kumar, H.L. Bassi, J. Seng, Barber, L.H. Wong, ACS Appl. Mater. Interfaces **6**, 5852 (2014)
3. H. Hsu, L. Ji, H.S. Ahn, J. Zhao, E.T. Yu, A.J. Bard, J. Am. Chem. Soc. **137**, 14758 (2015)
4. S.Y. Tee, K.Y. Win, W.S. Teo, L.D. Koh, S. Liu, C.P. Teng, M.Y. Han, Adv. Sci. **4**, 1600337 (2017)
5. T. Hong, Z. Liu, H. Liu, J. Liu, X. Zhang, J. Han, K. Guo, B. Wang, J. Mater. Chem. A **3**, 4239 (2015)
6. K. Keis, L. Vayssieres, H. Rensmo, S.-E. Lindquist, A. Hagfeldt, J. Electrochem. Soc. **148**, A149 (2001)
7. Z. Zhang, P. Wang, J. Mater. Chem. **22**, 2456 (2012)
8. A. Paracchino, V. Laporte, K. Sivula, M. Grätzel, E. Thimsen, Nat. Mater. **10**, 456 (2011)
9. S.U.M. Khan, M. Al-Shahry, W.B. Ingler, Science **297**, 2243 (2002)
10. I.S. Cho, C.H. Lee, Y. Feng, M. Logar, P.M. Rao, L. Cai, D.R. Kim, R. Sinclair, X. Zheng, Nat. Commun. **4**, 1723 (2013)
11. J. Lin, P. Hu, Y. Zhang, M. Fan, Z. He, C.K. Ngaw, J.S.C. Loo, D. Liao, T.T.Y. Tan, RSC Adv. **3**, 9330 (2013)
12. Y. Liu, J. Li, W. Li, Y. Yang, Y. Li, Q. Chen, J. Phys. Chem. C **119**, 14834 (2015)
13. S.P. Berglund, D.W. Flaherty, N.T. Hahn, A.J. Bard, C.B. Mullins, J. Phys. Chem. C **115**, 3794 (2011)
14. P.S. Archana, Z. Shan, S. Pan, A. Gupta, Int. J. Hydrog. Energy **42**, 8475 (2017)
15. M. Chakraborty, D. Roy, A. Biswas, R. Thangavel, G. Udayabhanu, RSC Adv. **6**, 75063 (2016)
16. Y. Wang, Y.Z. Zheng, S. Lu, X. Tao, Y. Che, J.F. Chen, ACS Appl. Mater. Interfaces **7**, 6093 (2015)
17. F. Wang, L. Song, H. Zhang, L. Luo, D. Wang, J. Tang, J. Electron. Mater. **46**, 4716 (2017)

18. A. Wolcott, W.A. Smith, T.R. Kuykendall, Y. Zhao, J.Z. Zhang, Adv. Funct. Mater. **19**, 1849 (2009)
19. W.-K. Hong, J.I. Sohn, D.-K. Hwang, S.-S. Kwon, G. Jo, S. Song, S.-M. Kim, H.-J. Ko, S.-J. Park, M.E. Welland, T. Lee, Nano Lett. **8**, 950 (2008)
20. M. Gratzel, Nature **414**, 338 (2001)
21. N.M. Vuong, J.L. Reynolds, E. Conte, Y.I. Lee, J. Phys. Chem. C **119**, 24323 (2015)
22. A. Soudi, P. Dhakal, Y. Gu, Appl. Phys. Lett. **96**, 2008 (2010)
23. W.I. Park, D.H. Kim, S.W. Jung, G.C. Yi, Appl. Phys. Lett. **80**, 4232 (2002)
24. D.B. Potter, M.J. Powell, J.A. Darr, I.P. Parkin, C.J. Carmalt, RSC Adv. **7**, 10806 (2017)
25. L. Liang, Z. Huang, L. Cai, W. Chen, B. Wang, K. Chen, H. Bai, Q. Tian, B. Fan, ACS Appl. Mater. Interfaces **6**, 20585 (2014)
26. A.B. Djurišić, Y.H. Leung, K.H. Tam, L. Ding, W.K. Ge, H.Y. Chen, S. Gwo, Appl. Phys. Lett. **88**, 103107 (2006)
27. H. Yuan, J. Mater. Sci. **23**, 2075 (2012)
28. S.N. Sarangi, J. Phys. D **49**, 355103 (2016)
29. M.J. Height, L. Mädler, S.E. Pratsinis, F. Krumeich, Chem. Mater. **18**, 572 (2006)
30. K.H. Tam, C.K. Cheung, Y.H. Leung, A.B. Djurišić, C.C. Ling, C.D. Beling, S. Fung, W.M. Kwok, W.K. Chan, D.L. Phillips, L. Ding, W.K. Ge, J. Phys. Chem. B **110**, 20865 (2006)
31. Y. Yang, S. Niu, D. Han, T. Liu, G. Wang, Y. Li, Adv. Energy Mater. **7**, 1 (2017)
32. C.L. Hsu, S.J. Chang, Small **10**, 4562 (2014)
33. F.X. Xiao, J. Miao, H.B. Tao, S.F. Hung, H.Y. Wang, H.Bin Yang, J. Chen, R. Chen, B. Liu, Small **11**, 2115 (2015)
34. C.F. Liu, Y.J. Lu, C.C. Hu, ACS Omega **3**, 3429 (2018)
35. J. Wang, T. Tsuzuki, L. Sun, X. Wang, ACS Appl. Mater. Interfaces **2**, 957 (2010)
36. R. Chowdhury, S. Adhikari, P. Rees, Phys. B Condens. Matter **405**, 4763 (2010)
37. X. An, G. Meng, Q. Wei, L. Zhang, Cryst. Growth Des. **6**, 1967 (2006)
38. A.P. Goodey, S.M. Eichfeld, K.-K. Lew, J.M. Redwing, T.E. Mallouk, J. Am. Chem. Soc. **129**, 12344 (2007)
39. J. Zhao, L. Qin, L. Zhang, Phys. E **40**, 795 (2008)
40. T. Minami, H. Sato, H. Nanto, S. Takata, Jpn. J. Appl. Phys. **25**, L776 (1986)
41. W. Körner, C. Elsässer, Phys. Rev. B **83**, 1 (2011)
42. H.C. Wu, Y.C. Peng, T.P. Shen, Materials **5**, 2088 (2012)
43. J. Clatot, M. Nistor, A. Rougier, Thin Solid Films **531**, 197 (2013)
44. R. Thangavel, R. Singh Moirangthem, W.S. Lee, Y.C. Chang, P.K. Wei, J. Kumar, J. Raman Spectrosc. **41**, 1594 (2010)
45. M. Chakraborty, P. Mahapatra, R. Thangavel, Thin Solid Films **612**, 49 (2016)
46. I. Sorar, D. Saygin-Hinczewski, M. Hinczewski, F.Z. Tepehan, Appl. Surf. Sci. **257**, 7343 (2011)
47. A. Sharma, M. Chakraborty, R. Thangavel, G. Udayabhanu, J. Sol-Gel. Sci. Technol. **85**, 1 (2018)
48. M. Subramanian, P. Thakur, S. Gautam, K.H. Chae, M. Tanemura, T. Hihara, S. Vijayalakshmi, T. Soga, S.S. Kim, K. Asokan, R. Jayavel, J. Phys. D **42**, 105410 (2009)
49. J. Clatot, G. Campet, A. Zeinert, C. Labrugère, M. Nistor, A. Rougier, Sol. Energy Mater. Sol. Cells **95**, 2357 (2011)
50. S.A. Ansari, A. Nisar, B. Fatma, W. Khan, A.H. Naqvi, Mater. Sci. Eng. B **177**, 428 (2012)
51. R.O. Yathisha, Y. Arthoba Nayaka, J. Mater. Sci. **53**, 678 (2018)
52. E. Chason, P.R. Guduru, J. Appl. Phys. **119**, 191101 (2016)
53. J.E. Allen, E.R. Hemesath, D.E. Perea, J.L. Lensch-Falk, Z.Y. Li, F. Yin, M.H. Gass, P. Wang, A.L. Bleloch, R.E. Palmer, L.J. Lauhon, Nat. Nanotechnol. **3**, 168 (2008)
54. F.-Y. Wang, Q.-D. Yang, G. Xu, N.-Y. Lei, Y.K. Tsang, N.-B. Wong, J.C. Ho, Nanoscale **3**, 3269 (2011)
55. L. Song, L. Luo, J. Song, H. Zhang, X. Li, S. Cheng, W. Jin, J. Tang, L. Liu, F. Wang, Catalysts **7**, 371 (2017)
56. A.P. Roth, J.B. Webb, D.F. Williams, Phys. Rev. B **25**, 7836 (1982)
57. E. Burstein, Phys. Rev. **93**, 632 (1954)
58. T.S. Moss, Phys. Status Solid **131**, 415 (1985)
59. S. Klubnuan, S. Suwanboon, P. Amornpitoksuk, Opt. Mater. **53**, 134 (2016)
60. J.P. Dhal, B.G. Mishra, G. Hota, RSC Adv. **5**, 58072 (2015)
61. H. Gerischer, J. Electroanal. Chem. **82**, 133 (1977)
62. H. Gerischer, N. Sorg, Electrochim. Acta **37**, 827 (1992)
63. K. Sun, K. Madsen, P. Andersen, W. Bao, Z. Sun, D. Wang, Nanotechnology **23**, 194013 (2012)